

The Multiple Extended Tidal Tails of NGC 288

CARL J. GRILLMAIR¹

¹*IPAC, California Institute of Technology, Pasadena, CA 91125*

ABSTRACT

Using photometry and proper motions from Pan-STARRS, DECaLS, and Gaia DR3, we detect a $\sim 35^\circ$ to 70° -long trailing stellar debris stream associated with the globular cluster NGC 288. The trajectory of the trailing tail is not well matched by a model stream evolved in a static Galactic potential, but is reasonably well-matched by a stream modeled in a potential that incorporates a massive, infalling Large Magellanic Cloud. We also detect a broad, at least $\sim 40^\circ$ -long leading tail that appears to be composed of at least two narrower, spatially offset, and kinematically distinct streams. Stream modeling predicts a similar broad composite of streams and suggests that these narrower components could each be made up of one or more generations of tidal tails, each formed during different orbits over the past few gigayears. On the other hand, NGC 288 is believed to have been brought into the Galactic halo during the Gaia-Enceladus-Sausage accretion event, and the tangential velocity dispersions of our stream candidates are indeed most consistent with having been stripped in a parent galaxy that had a large, cored dark matter halo. Tables of the most highly ranked stream star candidates are provided for ongoing and future spectroscopic surveys.

Keywords: Galaxy: Structure — Galaxy: Halo — Globular Clusters: general — Globular Clusters: individual (NGC 288)

1. INTRODUCTION

Recent years have seen an enormous increase in the number of distinct stellar debris streams detected in the Galactic halo (Grillmair & Carlin 2016; Shipp et al. 2018; Malhan et al. 2018; Ibata et al. 2019, 2021; Mateu 2023). A large number of these streams appear to be quite narrow, with physical widths on the order of 100 pc, and are believed to have been generated by globular clusters (GCs) formed *in situ*. Zhang et al. (2022) compiled a catalog of globular clusters with robust detections of tidal tails or extra-tidal structures. Grondin et al. (2024) have recently computed positions and velocities of tidally stripped mock stars for all 159 globular clusters in the catalog of Baumgardt & Hilker (2018). Thin, cold streams are particularly sensitive to interactions with dark matter subhalos (Carlberg 2009; Yoon et al. 2011; Erkal et al. 2016), though episodic tidal stripping and associated variations in stream density complicate the search for direct evidence of such interactions (Küpper et al. 2012; Thomas et al. 2016).

On the other hand, by having well-characterized progenitors, tidal tails associated with GCs will be useful for understanding the detailed physics of tidal stripping (Balbinot & Gieles 2018), the accretion sequence of the halo, and the shape of the Galactic potential (Bovy et al. 2016; Price-Whelan et al. 2014; Malhan & Ibata 2019; Garavito-Camargo et al. 2021). Longer streams and streams on more eccentric orbits are particularly sensitive to the shape of the halo potential (Bonaca & Hogg 2018). Carlberg (2018) and Malhan et al. (2021, 2022) showed that the spatial widths and velocity dispersions of GC tidal tails should be significantly larger for GCs that originated in and were initially stripped by infalling satellite galaxies with cored or cuspy cold dark matter halos. For all these reasons, it would be extremely useful to trace GC streams as deeply and as far around the Galaxy as the data will allow.

With accurate stellar proper motions over the entire sky, the third data release (DR3) of the Gaia catalog (Gaia Collaboration et al. 2023) has made it possible to detect stellar debris streams to far lower surface densities than was possible with the purely photometric catalogs of the pre-Gaia era (Malhan & Ibata 2018; Malhan et al. 2018;

Grillmair 2019; Ibata et al. 2019, 2021; Grillmair 2022; Yang et al. 2023). In our ongoing effort to extend individual globular cluster tidal streams as far across the sky as possible, we focus here on the old, metal poor globular cluster NGC 288.

The extended envelope and incipient tidal tails of NGC 288 were first detected in the photographic work of Grillmair et al. (1995) and were among the strongest detections in their sample. Leon et al. (2000) and Piatti (2018) later found even more extensive extra-tidal structures surrounding the cluster. Shipp et al. (2018), Kaderali et al. (2019), and Sollima (2020) found a strong, wide plume of stars extending up to 6° to the south of NGC 288 and, most recently, Ibata et al. (2021) used STREAMFINDER (Malhan & Ibata 2018) to detect a narrow trailing tail extending some 8° to the northwest of the cluster.

In this work we combine Gaia DR3 with two ground-based photometric catalogs to push the known limits of NGC 288’s tidal tails even further. Section 2 describes our method, which largely mirrors that used by Grillmair (2019) and Grillmair (2022) to detect the extended tails of M5 and M2, respectively. We discuss the apparent trajectories, morphology, and dynamical widths of NGC 288’s tails in Section 3. We also provide tables of our most highly ranked stream star candidates. We make concluding remarks in Section 4.

2. ANALYSIS

Our analysis generally follows that of Grillmair (2019) (henceforth G19) and Grillmair (2022) (henceforth G22) as applied to the globular clusters M5 and M2, combining color-magnitude and proper motion filtering with orbit integrations and predictions based on modeling the stripping of stars from NGC 288. We make use of the photometry and proper motions contained in Gaia DR3 (Gaia Collaboration et al. 2023), DECaLS (Dey et al. 2019), and Pan-STARRS (Tonry et al. 2012; STScI 2022). We compute the expected proper motions and trajectories on the sky using the Galactic model of Allen & Santillan (1991), coded in the IDL language and updated using the parameters of Irrgang et al. (2013). The model includes a $6.6 \times 10^{10} M_\odot$ Miyamoto-Nagai disk (Miyamoto & Nagai 1975), a $9.5 \times 10^9 M_\odot$ spherical bulge, and a $1.8 \times 10^{12} M_\odot$ spherical halo. Our experience using it with other clusters (e.g. G19 and G22) suggests that it provides reasonably good approximations for actual cluster orbits in the inner halo.

It is now generally agreed (Kallivayalil et al. 2013; Erkal et al. 2019; Shipp et al. 2021) that the Large Magellanic Cloud (LMC) is considerably more massive than previously supposed and may be a significant perturber of satellite orbits. Following G22, we augmented our Galactic potential with a moving LMC, modeled as a point mass with $M = 1.88 \times 10^{11} M_\odot$ (Shipp et al. 2021) and arriving at its present location on a first pass. The LMC trajectory was modeled as a fall from ≈ 700 kpc, slowed by dynamical friction (Chandrasekhar 1943) according to the local density of stars and dark matter along its orbit. While the stellar/dark matter wake of the LMC is believed to be quite substantial (Conroy et al. 2021; Garavito-Camargo et al. 2021), we have not attempted to model it as an additional perturber on the orbit of NGC 288.

For modeling the orbit of NGC 288 and the motions of associated stream stars, we used a cluster distance of 8.988 ± 0.89 kpc (Baumgardt & Vasiliev 2021), cluster proper motions of $\mu_\alpha = 4.164 \pm 0.024$ mas yr $^{-1}$ and $\mu_\delta = -5.705 \pm 0.024$ mas yr $^{-1}$ (Vasiliev & Baumgardt 2021), and a radial (line-of-sight) velocity of -44.83 km sec $^{-1}$ (Vasiliev 2019). We computed the predicted trajectories of the tidal tails by modeling the release of stars from the cluster over time (Küpper et al. 2015; Bowden et al. 2015; Fardal et al. 2015; Dai et al. 2018; Grillmair 2022). Specifically, the model tails were generated by releasing stars from the cluster at a rate proportional to $1/R^3$, where R is the Galactocentric radius of the cluster at any point in time. Escaping stars were simply placed at the current ≈ 34 pc tidal radius of the cluster (Harris 1996), both at the L1 and L2 points, and then integrated independently along their individual orbits. Orbit integrations were run for the equivalent of 5 Gyr to provide tidal tails long enough to cover our field of interest. The results of our modeling are shown in Figure 1.

Also shown in Figure 1 is a simulation of stripped stars for NGC 288 by Grondin et al. (2024). While this simulation shows considerably more spread in all coordinates due to a longer integration time and to the inclusion of realistic three-body dynamics in the core of the cluster, there are identifiable tidal tails that match reasonably well with those in our models. There are small differences in the positional, velocity, and proper motion profiles at any given R.A., but this not unexpected given the different models used for the underlying Galactic potential. More importantly, the *shape* of the distance and proper motion profiles are very similar and, as we discuss below, we allow our distance and proper motion profiles to shift up and down to first discover and then to maximize the signal of stream stars.

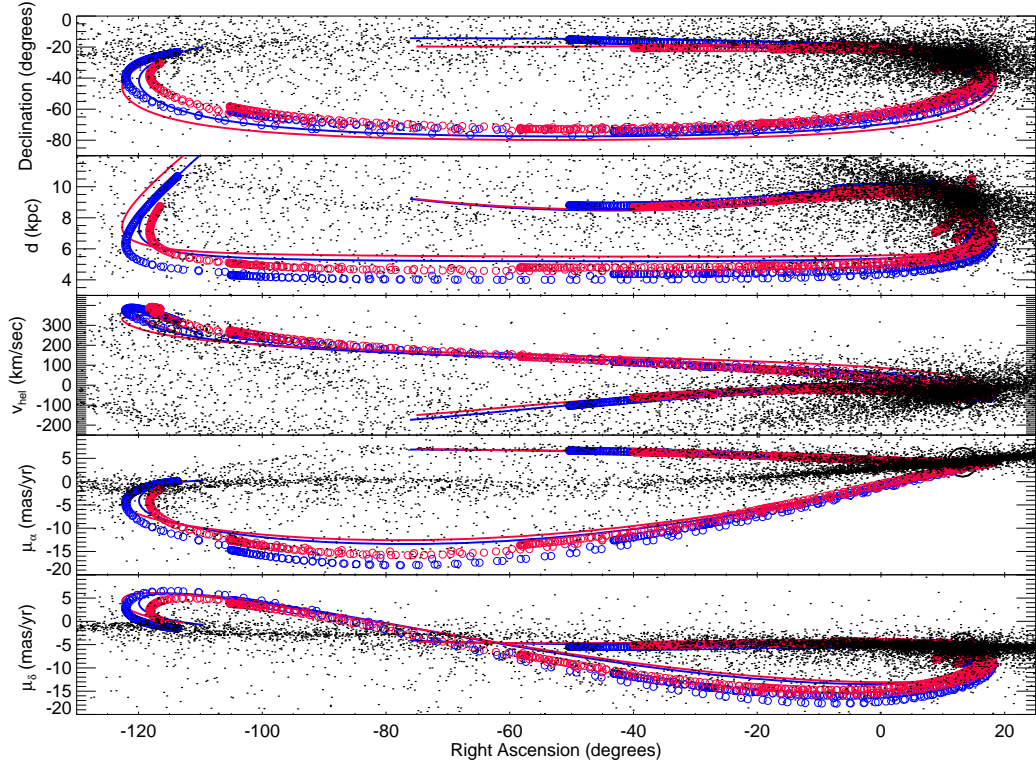


Figure 1. The run of declination, distance, radial (line-of-sight) velocity, and proper motions with Right Ascension for the orbit of NGC 288 and its tidal tails, as predicted using the Galactic model of Allen & Santillan (1991), updated with model parameters from Irrgang et al. (2013), and with or without a perturbing LMC. The solid curves show orbit integrations of NGC 288 itself, using just the Allen & Santillan (1991) model (blue curve) and supplemented by a point-mass LMC fixed at its current position with $M = 1.88 \times 10^{11} M_{\odot}$ (red curve). The small open circles show the results of sequentially releasing 2000 test particles from NGC 288’s L1 and L2 locations and integrating their orbits separately. The blue circles are test particles integrated using just the Galactic model, while the red circles include the effect of a massive LMC falling from 700 kpc to its current position on a first pass. The large black circles show the measured quantities for NGC 288 itself. The black dots show the distributions of single stars in the tidal stripping simulation for NGC 288 by Grondin et al. (2024).

To reduce contamination by foreground stars, we limited our analysis to stars with $15 < G < 20.0$. For stars fainter than $G = 20$, the Gaia photometry and proper motion uncertainties are large enough that their inclusion results in noticeably noisier results.

We used Gaia, Pan-STARRS, and DECaLS photometry to determine photometric membership probabilities for individual stars. We used a modified form of the matched filter described by Rockosi et al. (2002) and Grillmair (2009). Specifically, we weighted stars both by their position in the extinction-corrected $G_0, (G_{BP} - G_{RP})_0, G_0, (g_{PS1} - r_{PS1})_0, G_0, (g_{PS1} - i_{PS1})_0, G_0, (g_{Decam} - r_{Decam})_0,$ and $G_0, (g_{Decam} - i_{Decam})_0$ color-magnitude diagrams of NGC 288 using an error-weighted average. The G magnitudes were adjusted faintward or brightward by sky location to account for the predicted variation in the heliocentric distances of stars along the leading and trailing arms. Photometry was corrected for extinction using the reddening maps of Schlegel et al. (1998), themselves corrected using the prescription of Schlafly & Finkbeiner (2011), and using the Gaia DR2 coefficients derived by Gaia Collaboration et al. (2018), the Pan-STARRS coefficients provided by Tonry et al. (2012), and the DECaLS coefficients given at <https://www.legacysurvey.org/dr5/description/>.

We also weighted stars by their departures from the predicted proper motion profiles shown in Figure 1. Since the proper motions and heliocentric distances at any given R.A. are not unique, we imposed the predicted trajectories of the leading and trailing arms on the sky so that the photometric and proper motion filtering applied to any particular star would depend on which point along which arm it is closest to.

While Gaia DR3 parallax measurements are generally not very accurate at the distance of NGC 288, we carried out experiments using parallax as an additional constraint to weed out both foreground dwarfs and very distant stars or galaxies. These experiments showed a small but noticeable improvement in signal-to-noise ratio. All results shown here consequently employed an additional weighting factor based on the expected parallax at each point along each arm.

Stream membership probabilities were computed as a product of the CMD, μ_α , μ_δ , and parallax membership probabilities. We then summed the resulting filter signals by sky position to produce probability surface density maps we could examine for evidence of tidal streams. Several thousand orbit models were computed over a three-dimensional grid of distance, μ_α , and μ_δ . While the proper motions at every point along the tidal tails predicted by our relatively simple model of the Galactic potential are not terribly accurate, the overall *shape* of the proper motion profiles in Figure 1 are reasonably invariant over the range of uncertainties in NGC 288’s distance, proper motion, and radial velocity. We consequently shifted the proper motion profiles up and down by up to 5 mas yr^{-1} in increments of 0.1 mas yr^{-1} . Similarly, the distance profile in Figure 1 was shifted up and down by up to 1 kpc in increments of 200 pc. The resulting surface density maps were then examined by eye to look for obvious enhancements along the expected positions of the tidal tails.

We restricted our search to the Southern Galactic cap. Our models predict that NGC 288’s tidal arms do not extend much beyond 10° north of the Galactic plane. Moreover, the proper motions of tail stars north of the Galactic plane are predicted to be very close to zero and virtually indistinguishable from those of the field population.

3. DISCUSSION

Figure 2 shows clear plumes of stars emanating from NGC 288, both along the $l = 310^\circ$ meridian, and in the general direction of the $l = 130^\circ$ meridian. The northern portion of the very strong, 10° -long leading plume extending along the $l = 310^\circ$ meridian was detected by Shipp et al. (2018) in Dark Energy Survey data and by Kaderali et al. (2019) and Sollima (2020) in Gaia DR2. We refer to this feature as a plume (as distinct from a tidal tail) owing to its relative compactness, its $\sim 40^\circ$ misalignment with the expected orbit of the cluster and the track of the stream, and its similarity to relatively recent ejections of stars apparent in Figure 1. The stars in such plumes eventually spread out along their own orbits, creating new tidal tails that may or may not be easily distinguishable from previous generations (Hozumi & Burkert 2015).

To the upper left in Figure 2, the trailing plume is much broader, extending at least 20° from the cluster in a fan-shaped distribution. These stars are only slightly separated from one another in proper motion, and a sweep through proper motion space highlights different portions of the plume monotonically from one side to the other.

3.1. Leading Tail

There is a clear surplus of stars (detected at the $\sim 4\sigma$ level with respect to field stars using the T-statistic of Grillmair (2009)) extending at least 40° north of the cluster along the $l \sim 300^\circ$ meridian, and possibly up to $\approx 80^\circ$ from the cluster, where it becomes overwhelmed by the Galactic disk. This feature, which we will refer to as NGC 288’s leading tail, is in good accord with the trajectories of the leading tails predicted by models both with and without a massive, infalling LMC.

At roughly 5° across, the leading tail is quite broad. From Figure 1 we see that the leading tail passes within 6 kpc of the Sun on its way to perigalacticon. At this distance an apparent width of 5° would correspond to about 500 pc. This would be unusually broad compared with other presumed globular cluster streams (*e.g.* GD-1 and Pal 5). However, careful examination of the surface density maps in the 3-dimensional grid of μ_α , μ_δ , and distance shows that this leading tail is made up of at least two components, separated in proper motion by $\sim 1 \text{ mas yr}^{-1}$ in μ_α and $\sim 0.3 \text{ mas yr}^{-1}$ in μ_δ . Figure 3 shows surface density maps generated after appropriately offsetting the proper motions from the nominal values used for Figure 2. Each panel shows a $\approx 5\sigma$ excess of stars over the background, and the visible streams are laterally offset from one another by about 4° . The apparent widths of these sub-streams are each less than 2° , or about 200 pc.

For comparison, we show a 5000-particle model, run forward from a point 3 Gyr in the past, and including a massive infalling LMC in Figure 4. At $b = -60^\circ$, the different generations of leading tails produce a swath more than 5° across, in good agreement with the observed tail in Figure 2. The individual tails do not arrange themselves in any particular order; there are both older and younger generations of tails populating both the inner and outer regions of the swath. The formation of distinct tidal tails during each orbit has been examined in greater detail by Montuori et al. (2007)

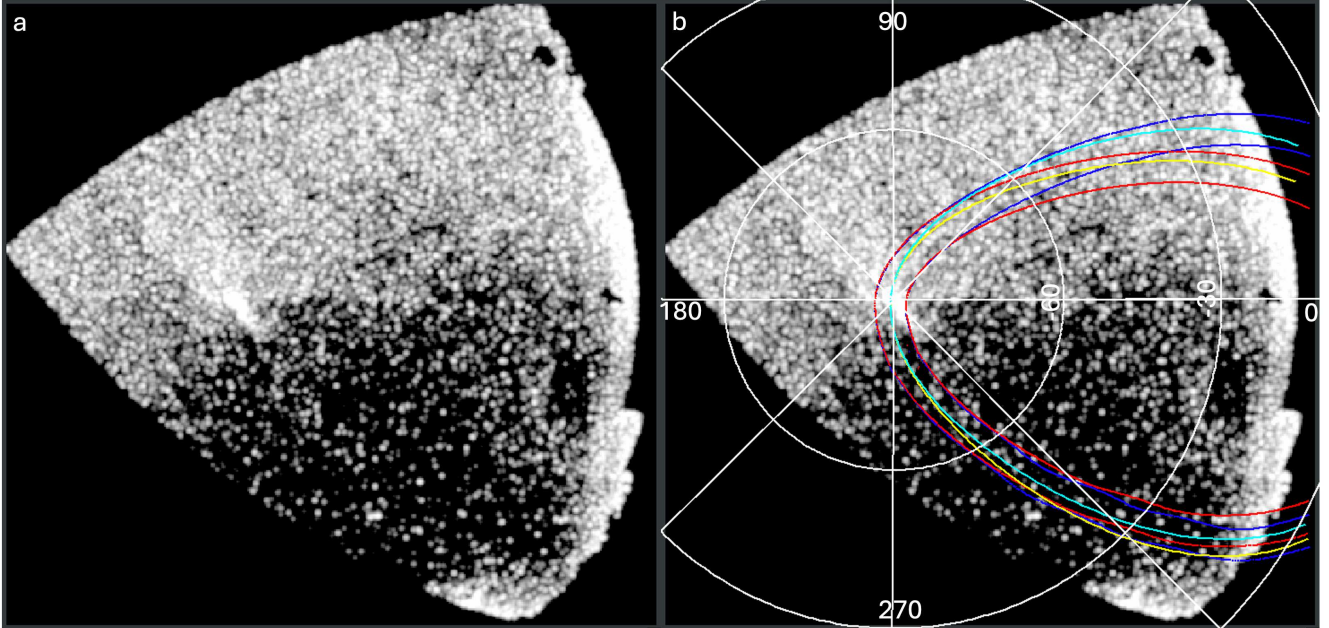


Figure 2. Probability surface density maps of NGC 288 and its tidal arms. This polar projection, centered on the south Galactic pole, encompasses $\approx 10,000$ square degrees, or roughly one quarter of the sky. The stretch is logarithmic, the scale is 0.3° per pixel, and the maps have been smoothed with a Gaussian kernel of 0.3° . The background discontinuities across the middle of the images are a consequence of applying different proper motion filters to areas near the leading and trailing tidal arms, respectively. Panel (b) is identical in scale and stretch to panel (a) but provides a Galactic coordinate grid along with an overlay of the cluster orbits and the model streams shown in Figure 1. The yellow and cyan curves show the orbit of NGC 288 itself, with and without a massive LMC, respectively. The red and blue curves are offset 3° from the centerlines of tidal tail models with and without a massive infalling LMC, respectively.

and Hozumi & Burkert (2015), among others. Though the physical widths of tidal tails are known to depend on the size and concentration of the galaxies in which a cluster first formed (Carlberg 2018; Malhan et al. 2021), our modeling suggests that the overall width of NGC 288’s leading tail could be a natural consequence of the precession of the cluster’s orbit in the aspherical potential of the Galaxy.

Averaging over the inner (western) and outer (eastern) streams in the model, we find that the proper motion offsets between the substreams in μ_α and μ_δ are about 0.2 mas yr^{-1} and 1.1 mas yr^{-1} , respectively. While similar in total magnitude to what we find observationally, these offsets are reversed in the sense that μ_α is the larger component of the offset. We attribute this disagreement to the limited fidelity of our model potential which, among many other things, does not include a bar or a Galactic wake due to perturbations by the LMC. Comparing photometric distances for candidate stars in the southern 40° of each stream (see below), we find a mean distance offset of $93 \pm 110 \text{ pc}$, in the sense that the outer (western) stream may be slightly closer to us than the inner (eastern) stream. Though consistent with zero, this offset agrees with with a $\approx 75 \text{ pc}$ offset, in the same sense, between the western and eastern halves of

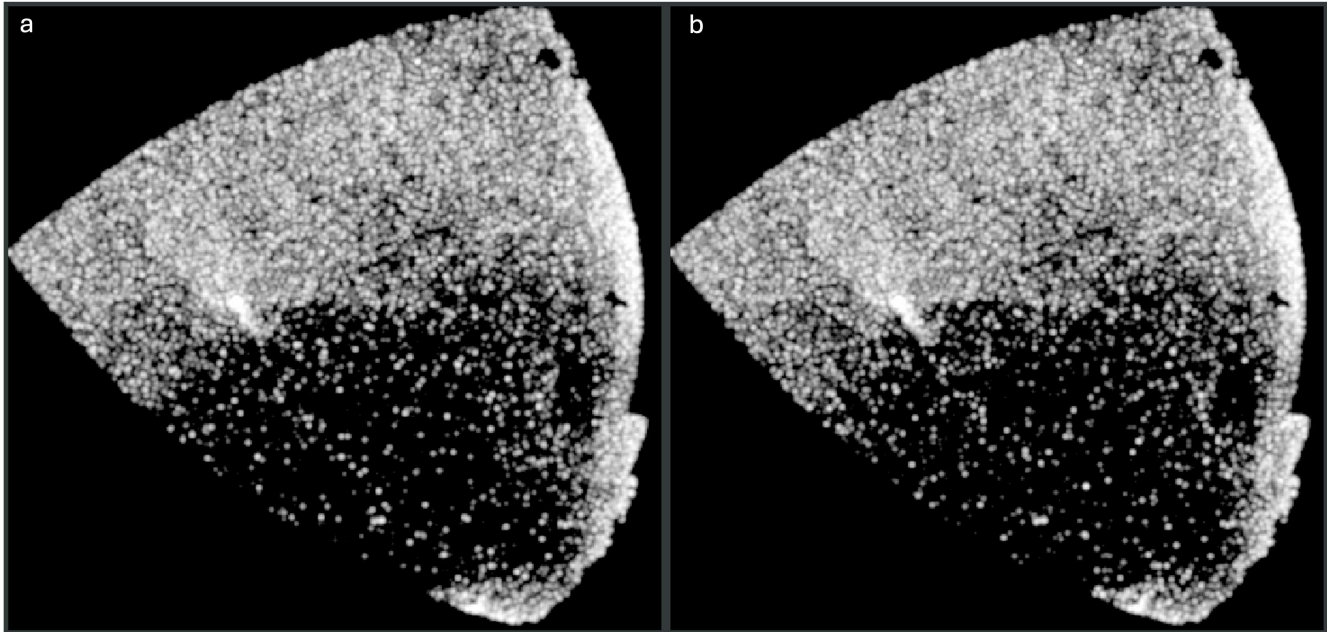


Figure 3. Same as Figure 2, but using proper motion profiles offset from one another by 1 mas yr^{-1} in μ_α and 0.3 mas yr^{-1} in μ_δ . Panel (a) shows a probability map computed for the “outer” leading stream, while panel (b) shows a map computed for the “inner” leading stream.

the model stream in Figure 4. Combined, these offsets support the notion that we are seeing multiple generations of tidal tails. While each of the streams visible in Figure 3 are likely made up of stars stripped during multiple orbits, for simplicity we henceforth refer to the stream in panel (a) of Figure 3 as the outer leading stream, and the stream in panel (b) as the inner leading stream.

3.2. *Trailing Tail*

NGC 288’s trailing tail extends to the upper right of the cluster in Figure 2 roughly along $l = 55^\circ$. The first 8° of this tail was detected by [Ibata et al. \(2021\)](#). The extended trailing tail in Figure 2, while more contaminated by foreground stars with similar proper motions than the leading tail, is detectable to $b \sim -55^\circ$. Beyond that the signal becomes more tenuous, essentially disappearing in the region $-58^\circ < b < -48^\circ$, and apparently resurging in the region $-40^\circ < b < -25^\circ$. Over the interval $-90^\circ < b < -25^\circ$ the stream is detected at the 4.7σ level. The trailing tail appears somewhat narrower on the sky than the leading tail, with a full-width-at-half-maximum of about 1.5° . At a distance of between 8.6 and 9.4 kpc, this corresponds to a physical width of between 200 and 250 pc. Interestingly, this narrower profile is also reflected in the model tails in Figure 4, with different generations of trailing tails nearly overlapping from our Galactic vantage point.

The trailing tail is reasonably well matched in position by a stream model incorporating a massive infalling LMC (Figure 2). On the other hand, the trajectory predicted by a model without an infalling LMC departs fairly quickly

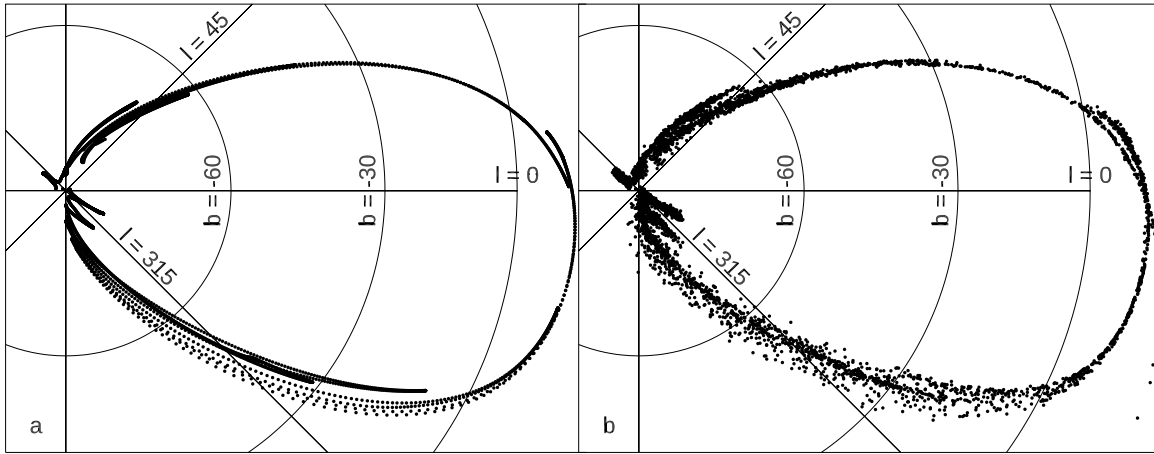


Figure 4. A model of NGC 288’s tidal tails after running for the equivalent of 3 Gyr in a Galactic potential that incorporates a massive infalling LMC. Panel (a) shows a model in which stripped stars have zero velocity dispersion at the time of release. Panel (b) shows results for the same model, but with stars that are given a velocity dispersion of 1 km s^{-1} at the time of release. The projection and orientation are identical to those used in Figures 2 and 3.

from that of the observed stream. This is qualitatively similar to the results of G22 for NGC 7089, who found that both the trajectory and the proper motions of NGC 7089’s observed trailing tail were better matched by a model incorporating a massive infalling LMC.

3.3. Candidate Tail Stars

Gaia DR3 radial velocities extend to $G_{RVS} \approx 14$ (Katz et al. 2023), which unfortunately is considerably brighter than our brightest high-probability candidate ($G = 17.8$). A positional matching of our highest-weighted stars with the Sloan Digital Sky Survey Data Release 15 (Aguado et al. 2019) as well as the LAMOST Data Release 6 (Zhao et al. 2012) did not yield any radial velocity measurements. To enable radial velocity follow-up measurements by the community, Tables 1, 2, and 3 list stars with the highest filter signals and lying along the trailing, outer leading, and inner leading tails, respectively. Each table is sorted by increasing Galactic latitude. Only stars with membership probabilities exceeding 0.22 (which would correspond to a star 1σ from the expected color-magnitude locus and 1σ from each of the expected μ_α and μ_δ profiles at any position along the stream) are listed in the tables. Distances are estimated by fixing the proper motion profiles at their “best” values, running the analysis over a range of assumed distances and determining the distance at which agreement between a star’s color and the expected color-magnitude locus at that sky position is maximized. Distance uncertainties are estimated by noting the distances at which the maximum CMD membership probability drops by a factor of 0.607 and thus correspond roughly to 1σ errors. In instances where stars could be either main sequence or subgiant stars, we choose the distance that best matches expectations for stream stars at that sky location, though the uncertainty is increased to reflect this degeneracy. Both leading and trailing tails become almost indistinguishable from the background near the Galactic plane. The positions, proper motions, and distances of all tabulated stars are plotted in Figures 5 and 6.

Table 1. Candidate Stream Stars: Trailing Tail

No.	R.A. (J2016)	dec (J2016)	G	$G_{BP} - G_{RP}$	$\mu_\alpha \cos \delta$ (mas yr $^{-1}$)	μ_δ (mas yr $^{-1}$)	Distance (kpc)	Probability
1	11.6178	-25.4231	19.846	0.849	4.519 ± 0.500	-4.652 ± 0.444	9.76 ± 1.56	0.78
2	10.5210	-25.2142	19.778	0.846	4.433 ± 0.481	-4.402 ± 0.405	8.12 ± 0.88	0.40
3	9.2878	-23.6151	19.271	0.686	5.240 ± 0.369	-4.006 ± 0.248	9.20 ± 1.52	0.34
4	8.8291	-24.0366	20.015	0.619	4.435 ± 0.582	-3.868 ± 0.659	8.31 ± 0.83	0.36

Table 1 continued on next page

Table 1 (continued)

No.	R.A. (J2016)	dec (J2016)	G	$G_{BP} - G_{RP}$	$\mu_{\alpha} \cos \delta$ (mas yr ⁻¹)	μ_{δ} (mas yr ⁻¹)	Distance (kpc)	Probability
5	8.1098	-24.0821	18.781	0.693	4.847 ± 0.205	-4.534 ± 0.261	10.31 ± 0.50	0.24
6	8.1033	-22.9501	19.944	0.773	5.287 ± 0.698	-4.241 ± 0.598	9.94 ± 1.48	0.76
7	6.5142	-22.9660	19.231	0.668	5.068 ± 0.336	-3.781 ± 0.254	8.16 ± 1.18	0.35
8	5.0590	-22.2461	19.979	0.735	4.564 ± 0.543	-4.037 ± 0.461	8.72 ± 0.94	0.51
9	4.6430	-22.2799	19.821	0.712	4.894 ± 0.451	-4.184 ± 0.440	9.32 ± 1.34	0.82
10	3.2104	-22.3650	19.018	0.666	5.036 ± 0.332	-4.233 ± 0.204	9.20 ± 1.41	0.42
11	1.8234	-21.6370	19.543	0.896	5.129 ± 0.389	-4.156 ± 0.297	8.26 ± 1.19	0.59
12	2.2048	-20.9640	19.054	0.731	5.021 ± 0.294	-3.937 ± 0.245	9.38 ± 2.25	0.82
13	0.5652	-20.8605	19.811	0.668	5.664 ± 1.106	-3.868 ± 0.565	10.78 ± 1.62	0.55
14	359.2597	-20.3508	19.864	0.775	5.923 ± 0.602	-3.600 ± 0.378	9.33 ± 1.20	0.29
15	357.6157	-20.7251	19.921	0.882	5.545 ± 0.468	-3.488 ± 0.544	9.00 ± 1.06	0.54
16	356.5639	-20.1499	19.467	0.880	5.259 ± 0.327	-3.663 ± 0.344	10.25 ± 1.80	0.75
17	353.7707	-20.0313	19.243	0.679	5.212 ± 0.304	-3.416 ± 0.334	8.83 ± 1.47	0.68
18	351.7619	-20.9221	18.938	0.639	5.619 ± 0.360	-3.305 ± 0.278	8.83 ± 1.26	0.41
19	351.7529	-18.6240	19.999	0.632	5.910 ± 0.573	-3.725 ± 0.552	7.77 ± 0.72	0.36
20	349.4342	-20.2762	19.877	0.857	5.560 ± 0.644	-3.417 ± 0.565	8.19 ± 0.85	0.79
21	348.5678	-20.0669	17.930	0.902	5.478 ± 0.129	-3.438 ± 0.116	8.14 ± 0.49	0.35
22	344.9409	-19.9379	19.995	0.819	5.670 ± 0.503	-3.871 ± 0.520	8.29 ± 0.83	0.60
23	343.1269	-20.4930	20.020	0.981	6.307 ± 0.622	-4.078 ± 0.664	7.93 ± 0.75	0.34
24	342.3369	-20.6402	19.578	0.755	5.842 ± 0.483	-3.792 ± 0.399	8.33 ± 1.25	0.55
25	341.0597	-20.5189	20.060	0.704	5.989 ± 0.637	-3.954 ± 0.554	9.15 ± 1.00	0.38
26	340.1381	-20.5307	20.056	0.870	5.674 ± 0.495	-3.143 ± 0.490	7.98 ± 0.75	0.49
27	336.1360	-20.3584	19.987	0.830	5.469 ± 0.524	-3.748 ± 0.468	8.03 ± 0.81	0.24
28	335.3248	-19.4792	19.796	0.871	6.716 ± 0.475	-3.188 ± 0.400	7.73 ± 1.01	0.37
29	333.2042	-20.3747	19.604	0.846	6.342 ± 0.336	-3.682 ± 0.318	8.36 ± 1.37	0.52
30	332.0131	-21.0193	18.772	0.662	6.316 ± 0.292	-3.124 ± 0.209	8.22 ± 1.27	0.39
31	329.8831	-20.6390	19.064	0.701	6.226 ± 0.291	-3.307 ± 0.287	7.40 ± 1.19	0.41
32	329.1082	-20.6083	19.098	0.603	6.747 ± 0.299	-2.988 ± 0.339	9.55 ± 1.51	0.24
33	327.7895	-20.6783	19.401	0.745	6.568 ± 0.517	-2.969 ± 0.389	8.40 ± 1.55	0.44
34	326.1528	-21.1658	18.878	0.700	6.532 ± 0.300	-3.684 ± 0.253	8.51 ± 2.21	0.39
35	324.6987	-20.5853	19.966	0.624	7.471 ± 0.791	-3.897 ± 0.462	8.34 ± 0.87	0.48
36	323.8435	-20.5527	18.646	0.717	6.983 ± 0.224	-3.342 ± 0.164	7.57 ± 1.52	0.74
37	322.6260	-20.5994	19.182	0.772	7.369 ± 0.376	-3.424 ± 0.280	7.49 ± 0.99	0.32
38	320.6786	-21.0356	19.617	0.936	6.599 ± 0.625	-3.702 ± 0.360	6.95 ± 0.72	0.29
39	319.8177	-21.5507	19.914	0.874	7.968 ± 0.672	-3.411 ± 0.747	8.43 ± 0.93	0.34
40	318.3910	-20.9930	19.765	0.765	7.257 ± 0.582	-3.867 ± 0.411	7.68 ± 0.79	0.75
41	315.4156	-22.1397	19.953	0.977	6.672 ± 0.625	-4.029 ± 0.471	7.61 ± 0.75	0.34
42	313.9588	-21.9383	18.394	0.806	7.417 ± 0.190	-3.670 ± 0.160	7.66 ± 0.50	0.82
43	310.2284	-22.2375	19.955	0.706	7.753 ± 0.436	-3.834 ± 0.356	8.05 ± 0.79	0.73
44	308.7216	-22.8732	18.726	0.714	7.743 ± 0.251	-3.472 ± 0.185	7.86 ± 1.97	0.35
45	309.1761	-21.1555	20.015	0.903	7.688 ± 0.564	-3.547 ± 0.387	7.65 ± 0.72	0.77

Table 1 continued on next page

Table 1 (*continued*)

No.	R.A. (J2016)	dec (J2016)	G	$G_{BP} - G_{RP}$	$\mu_{\alpha} \cos \delta$ (mas yr $^{-1}$)	μ_{δ} (mas yr $^{-1}$)	Distance (kpc)	Probability
46	307.1371	-22.0531	18.518	0.760	7.315 ± 0.206	-3.571 ± 0.145	6.88 ± 1.27	0.47
47	305.4191	-22.1641	19.826	0.801	7.012 ± 0.515	-3.437 ± 0.359	8.10 ± 0.97	0.52
48	304.5562	-22.1268	20.201	1.009	7.805 ± 0.766	-3.909 ± 0.578	8.10 ± 0.78	0.84
49	302.9991	-22.4355	20.342	1.101	8.514 ± 1.003	-4.168 ± 0.875	7.07 ± 0.80	0.27
50	301.5133	-22.5263	19.752	1.095	7.557 ± 0.440	-3.514 ± 0.305	7.45 ± 1.17	0.75
51	299.9524	-22.8098	18.765	0.767	7.415 ± 0.227	-3.652 ± 0.153	8.77 ± 0.56	0.78
52	300.2743	-21.8105	19.920	0.842	7.161 ± 0.589	-3.612 ± 0.327	7.89 ± 1.28	0.83
53	298.1937	-23.6058	19.271	0.854	7.490 ± 0.285	-3.815 ± 0.177	8.58 ± 1.50	0.44
54	296.9223	-23.4210	20.053	0.715	7.239 ± 0.917	-3.806 ± 0.791	7.67 ± 0.64	0.70
55	295.6508	-24.7409	18.670	0.795	7.444 ± 0.213	-3.393 ± 0.205	7.82 ± 1.71	0.78
56	295.2555	-24.3674	18.872	0.755	7.262 ± 0.214	-3.381 ± 0.197	8.79 ± 1.78	0.38
57	293.7054	-23.4103	20.142	0.882	7.395 ± 0.885	-4.003 ± 0.663	8.43 ± 1.28	0.71

Table 2. Candidate Stream Stars: Outer Leading Tail

No.	R.A. (J2016)	dec (J2016)	G	$G_{BP} - G_{RP}$	$\mu_{\alpha} \cos \delta$ (mas yr $^{-1}$)	μ_{δ} (mas yr $^{-1}$)	Distance (kpc)	Probability
1	16.1455	-29.0652	18.971	0.719	4.515 ± 0.192	-6.301 ± 0.318	9.01 ± 1.97	0.29
2	16.7313	-30.6763	19.696	0.758	4.180 ± 0.340	-6.386 ± 0.233	9.88 ± 1.41	0.43
3	13.6871	-35.0034	18.676	0.689	4.318 ± 0.120	-7.297 ± 0.127	7.96 ± 1.97	0.58
4	18.2333	-38.7918	19.679	0.775	4.176 ± 0.213	-8.204 ± 0.301	7.50 ± 0.71	0.38
5	16.9770	-43.4823	18.527	0.715	4.350 ± 0.097	-9.337 ± 0.106	7.62 ± 1.81	0.47
6	16.9643	-43.9691	18.113	0.669	4.315 ± 0.078	-9.680 ± 0.098	6.04 ± 1.09	0.52
7	17.0685	-44.8767	19.737	0.824	4.495 ± 0.220	-9.655 ± 0.297	6.49 ± 0.51	0.61
8	14.6984	-50.1758	19.969	0.857	3.961 ± 0.293	-11.429 ± 0.366	6.01 ± 0.40	0.23
9	13.3654	-50.5721	19.639	0.801	3.917 ± 0.227	-10.992 ± 0.277	5.81 ± 0.42	0.30
10	11.8523	-53.1060	19.058	0.000	4.138 ± 0.177	-11.667 ± 0.220	6.62 ± 0.82	0.27
11	16.8508	-54.0494	20.061	0.878	4.037 ± 0.401	-10.870 ± 0.517	6.20 ± 0.42	0.30
12	8.7388	-56.5193	19.299	0.761	3.338 ± 0.198	-12.359 ± 0.227	6.43 ± 0.62	0.75
13	11.9163	-59.4346	19.433	0.799	2.485 ± 0.241	-12.706 ± 0.268	5.54 ± 0.43	0.57
14	10.3915	-61.9728	19.419	0.900	2.175 ± 0.260	-12.785 ± 0.221	5.59 ± 0.44	0.55
15	7.5095	-63.8095	19.275	0.862	1.492 ± 0.274	-13.079 ± 0.232	5.48 ± 0.45	0.47
16	9.4180	-64.1045	18.997	0.782	2.062 ± 0.191	-13.123 ± 0.175	5.62 ± 0.55	0.22
17	6.2280	-68.3379	19.958	0.831	1.130 ± 0.391	-13.195 ± 0.374	5.40 ± 0.34	0.28
18	328.9156	-78.7878	19.248	0.915	-9.076 ± 0.255	-9.534 ± 0.278	5.46 ± 0.54	0.26
19	269.9732	-69.5896	19.412	0.867	-11.275 ± 0.166	1.886 ± 0.246	5.94 ± 0.55	0.35
20	261.2942	-70.4575	20.202	1.020	-11.118 ± 0.377	2.342 ± 0.473	6.12 ± 0.92	0.46
21	251.1577	-69.8245	20.092	1.063	-11.097 ± 0.313	2.790 ± 0.419	5.59 ± 0.87	0.39

Table 3. Candidate Stream Stars: Inner Leading Tail

No.	R.A. (J2016)	dec (J2016)	G	$G_{BP} - G_{RP}$	$\mu_\alpha \cos \delta$ (mas yr $^{-1}$)	μ_δ (mas yr $^{-1}$)	Distance (kpc)	Probability
1	13.8482	-29.7557	18.859	0.752	3.990 ± 0.199	-6.415 ± 0.279	8.58 ± 2.16	0.81
2	13.6004	-31.1579	19.506	0.704	4.045 ± 0.397	-6.617 ± 0.439	9.40 ± 1.44	0.79
3	12.8705	-32.5775	19.971	0.787	4.006 ± 0.561	-6.469 ± 0.649	8.38 ± 0.77	0.62
4	11.4731	-34.0426	19.965	0.915	3.951 ± 0.436	-6.905 ± 0.540	8.71 ± 0.82	0.62
5	12.3481	-34.9159	19.327	0.739	3.759 ± 0.169	-7.181 ± 0.348	8.35 ± 1.13	0.49
6	13.7741	-34.9398	19.612	0.724	3.664 ± 0.246	-7.390 ± 0.262	7.54 ± 0.76	0.48
7	11.9448	-35.7921	19.430	0.730	3.448 ± 0.219	-7.923 ± 0.376	8.45 ± 1.32	0.26
8	13.9332	-38.0415	18.671	0.678	3.667 ± 0.121	-8.461 ± 0.131	7.94 ± 1.49	0.26
9	11.8116	-39.5032	19.869	0.908	3.421 ± 0.262	-8.583 ± 0.306	7.36 ± 0.60	0.48
10	13.1899	-40.2668	19.151	0.669	3.762 ± 0.178	-8.480 ± 0.168	8.01 ± 1.06	0.38
11	13.3119	-40.9599	19.248	0.762	3.668 ± 0.196	-8.962 ± 0.204	7.31 ± 1.01	0.53
12	13.5271	-45.7569	17.825	0.686	3.551 ± 0.066	-10.039 ± 0.078	5.90 ± 1.10	0.04
13	10.7279	-47.0248	17.987	0.672	3.147 ± 0.063	-10.483 ± 0.085	6.20 ± 0.87	0.22
14	11.3402	-48.8570	18.518	0.655	3.257 ± 0.105	-11.108 ± 0.132	7.02 ± 1.50	0.24
15	7.1764	-55.6117	19.088	0.848	2.486 ± 0.158	-12.341 ± 0.207	6.15 ± 0.68	0.30
16	4.9437	-60.5060	19.711	0.943	0.966 ± 0.369	-13.155 ± 0.401	5.57 ± 0.38	0.33
17	357.0915	-62.6104	19.892	1.055	0.054 ± 1.306	-11.432 ± 1.456	5.37 ± 0.34	0.26
18	1.6782	-63.8208	18.475	0.733	0.255 ± 0.126	-12.895 ± 0.130	5.58 ± 0.70	0.75
19	344.4885	-70.5853	18.774	0.829	-4.093 ± 0.142	-13.240 ± 0.163	5.27 ± 0.59	0.33
20	333.3888	-70.3340	19.559	0.865	-6.382 ± 0.282	-12.352 ± 0.285	5.48 ± 0.40	0.25
21	261.2942	-70.4575	20.202	1.020	-11.118 ± 0.377	2.342 ± 0.473	6.12 ± 0.92	0.32
22	260.9115	-66.2357	19.970	0.958	-10.649 ± 0.275	3.467 ± 0.363	6.23 ± 1.30	0.53
23	257.3220	-63.6728	20.198	1.088	-9.199 ± 0.305	5.081 ± 0.374	5.68 ± 0.85	0.38

3.4. On the Origin of NGC 288

Using a chemo-dynamical technique to assign origins to much of the Galaxy’s globular cluster population, Callingham et al. (2022) determined a high probability that NGC 288 was brought into the halo during the Gaia-Enceladus-Sausage accretion event (Belokurov et al. 2018; Helmi et al. 2018). Malhan et al. (2021) and Malhan et al. (2022) demonstrated that the tidal tails of globular clusters should show morphological and dynamical differences depending on whether they formed *in situ* or whether they developed in either cored or cuspy dark matter halos of infalling satellite galaxies. Their modeling yielded remarkably distinct ranges for the physical widths and velocity dispersions of stream stars one should expect in each case. To determine whether our extended tidal tails are consistent with an infall picture, and perhaps further elucidate the nature of the halo of origin, we examine these quantities for the different sub-streams in our sample.

Using the highest probability candidates selected above, we measured the physical widths of the trailing tail, each of the leading tails, and both leading tails combined. Following Malhan et al. (2021), we break the tails into two to four segments and use our uncertainty-weighted photometric distance estimates to determine mean distances for each segment. We then measure the dispersion in the ϕ_2 coordinates to estimate the mean 1σ width for each tail. Similarly, after fitting and removing a ν_{tan} fit (where ν_{tan} derives from the quadrature sum of μ_α and μ_δ) we measure the dispersions in ν_{tan} . The uncertainties are estimated by computing thousands of realizations of possible distributions over $\sigma_{\nu_{tan}}$, given the distribution of proper motion uncertainties among our selected stars, and noting the upper and lower bounds where the 1σ distributions would allow a match to the observed data. Finally we compute Malhan et al.

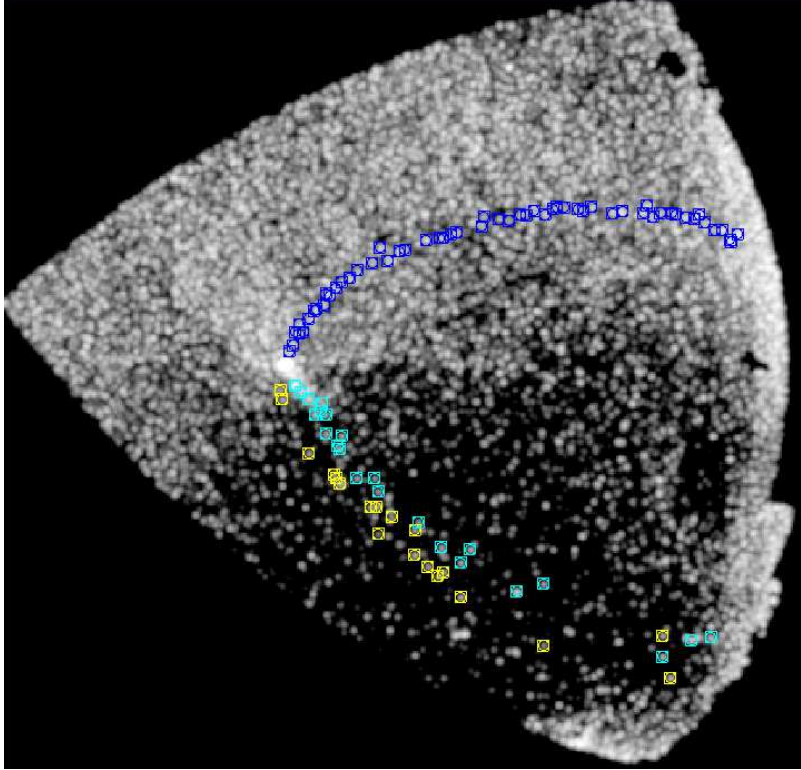


Figure 5. High-probability members of NGC 288’s tidal tails. The blue points show stars lying along the trailing tail, the cyan points designate candidate stars in the inner leading tail, and yellow points show stars we assign to the outer leading tail.

(2022)’s z scores (the differences between the observed and simulated velocity dispersions relative to the uncertainties) and their associated p values to determine the level of agreement between our measured quantities and those for the small/cuspy (SCu), large/cuspy, small/cored (SCo), and large/cored (LCo) parent galaxies that Malhan et al. (2022) modeled. We also compare our observed streams with the model stream shown in panel (b) of Figure 4. Table 4 lists these quantities for each of our extended tails individually, as well as for a combined leading tail that includes candidate stars from both inner and outer leading tails. We note that Malhan et al. (2022)’s *in situ* and large/cuspy halo simulations differ significantly from our observed tails, with $p < 10^{-3}$ in all cases, and are therefore not included in the table.

While the physical widths of the various streams are relatively narrow and seem to be more consistent with those found by Malhan et al. (2021) for streams formed *in situ*, our computed $\sigma_{\nu_{Tan}}$ values suggest that NGC 288 originally formed and evolved in a large/cored parent galaxy. This would be consistent with estimates for the mass of Gaia-Enceladus (*e.g.* Feuillet et al. (2020)). It is possible that we have been too conservative in selecting candidate stream stars, focusing on the strongest perceived stream signal in either a low surface density or a highly contaminated field of candidates. It would take only a few outliers to significantly inflate the 1σ widths of the streams. Expected future improvements in *Gaia*’s proper motion measurements along with radial velocity confirmations should eventually help us to better refine the sample and improve these estimates. The tangential velocity dispersions agree less well with the model streams in Figure 4 and with a small/cuspy halo origin, but we cannot rule either of them out at present.

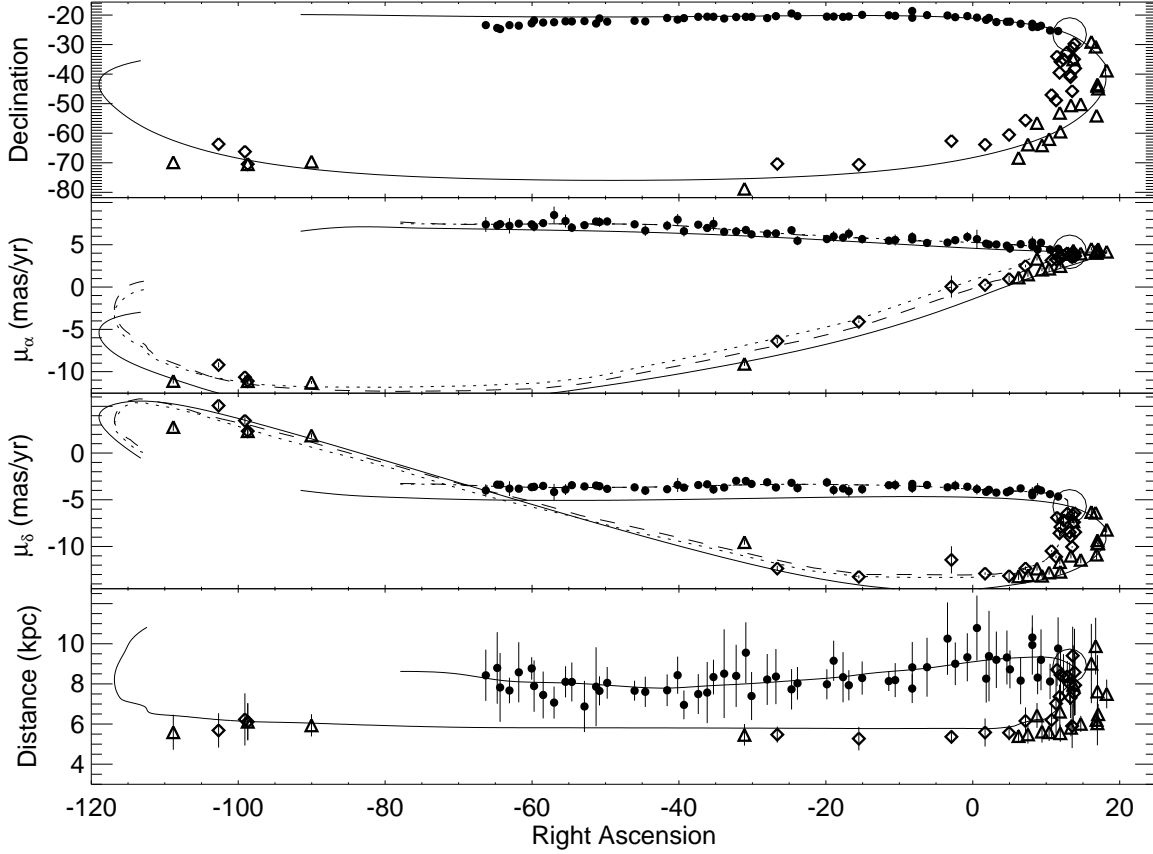


Figure 6. Positions, proper motions, and photometrically-estimated distances of our highest-ranked candidate tail stars, as listed in Tables 1, 2, and 3. The open circles denote NGC 288 itself. The filled circles show candidates in our trailing tail, while open triangles and open diamonds show candidates in our inner and outer leading tails, respectively. The solid curve is our nominal model of the positions, proper motions, and distances of stars in the tails based on our adopted Galactic model and a massive infalling LMC. The dashed and dotted curves are the offset proper motion profiles used to maximize the signal for the inner and outer streams, respectively.

Table 4. Physical Widths, Tangential Velocity Dispersions, and z Scores (with p values) for NGC 288’s Extended Tidal Tails

Tail	1σ Width (pc)	$\sigma_{v_{Tan}}$ (km s $^{-1}$)	SCu	SCo	LCo	Model Stream
Trailing	92	$3.04^{+0.56}_{-0.34}$	-1.11 (0.27)	3.18 (0.001)	0.89 (0.37)	1.65 (0.10)
Outer Leading	115	$2.70^{+1.2}_{-0.5}$	-0.82 (0.41)	1.89 (0.06)	0.54 (0.59)	-1.01 (0.31)
Inner Leading	89	$1.99^{+1.09}_{-0.43}$	-1.54 (0.12)	0.74 (0.46)	-0.74 (0.94)	-1.76 (0.08)
Combined Leading	182	$2.47^{+0.75}_{-0.39}$	-1.59 (0.11)	1.78 (0.08)	0.35 (0.73)	-1.91 (0.06)

4. CONCLUSIONS

Using Pan-STARRS, DECaLS, and Gaia DR3 photometry, proper motion, and parallax measurements we have detected both leading and trailing tidal tails of NGC 288. At surface densities well above the background, these tails extend at least 40° and 35° from the cluster, respectively. The leading tail appears to be composed of two or more spatially offset and kinematically distinct streams, in agreement with modeling results both here and in the literature.

While not as clearly distinct from field stars, highly probable NGC 288 member stars along the expected trajectories of the tails extend as far 80° and 70° from the cluster, respectively.

The physical widths of the tidal tails are somewhat narrower than one might expect if NGC 288 had originally formed in the fairly massive galaxy that led to the Gaia-Enceladus-Sausage event, but they appear to agree with the spread we see in multiple generations of tidal tails formed in an aspherical, LMC-perturbed Milky Way potential. On the other hand, the dispersions in the tangential velocities of our stream candidates are indeed more consistent with formation of the tails in a massive, cored satellite galaxy.

Verification of stream membership will require follow-up radial velocity measurements. If even a few of the most outlying candidates can be confirmed as having once belonged to NGC 288, this stream will become another particularly sensitive probe of the shape of the inner halo potential and an important contributor to our understanding of the influence of the LMC and other components of the Galaxy. Disentangling the different components of NGC 288's leading tidal tail in phase space should ultimately help us to better understand the process of weak tidal stripping, the history of the cluster's orbit, and the evolution of the Galactic potential over time.

We are grateful to an anonymous referee for several very useful suggestions that greatly improved the scope and content of the manuscript.

This work has made use of data from the European Space Agency (ESA) mission *Gaia* (<https://www.cosmos.esa.int/gaia>), processed by the *Gaia* Data Processing and Analysis Consortium (DPAC, <https://www.cosmos.esa.int/web/gaia/dpac/consortium>). Funding for the DPAC has been provided by national institutions, in particular the institutions participating in the *Gaia* Multilateral Agreement.

The Pan-STARRS1 Surveys (PS1) and the PS1 public science archive have been made possible through contributions by the Institute for Astronomy, the University of Hawaii, the Pan-STARRS Project Office, the Max-Planck Society and its participating institutes, the Max Planck Institute for Astronomy, Heidelberg and the Max Planck Institute for Extraterrestrial Physics, Garching, The Johns Hopkins University, Durham University, the University of Edinburgh, the Queen's University Belfast, the Harvard-Smithsonian Center for Astrophysics, the Las Cumbres Observatory Global Telescope Network Incorporated, the National Central University of Taiwan, the Space Telescope Science Institute, the National Aeronautics and Space Administration under Grant No. NNX08AR22G issued through the Planetary Science Division of the NASA Science Mission Directorate, the National Science Foundation Grant No. AST-1238877, the University of Maryland, Eotvos Lorand University (ELTE), the Los Alamos National Laboratory, and the Gordon and Betty Moore Foundation.

The DESI Legacy Imaging Surveys consist of three individual and complementary projects: the Dark Energy Camera Legacy Survey (DECaLS), the Beijing-Arizona Sky Survey (BASS), and the Mayall z-band Legacy Survey (MzLS). DECaLS, BASS and MzLS together include data obtained, respectively, at the Blanco telescope, Cerro Tololo Inter-American Observatory, NSF's NOIRLab; the Bok telescope, Steward Observatory, University of Arizona; and the Mayall telescope, Kitt Peak National Observatory, NOIRLab. NOIRLab is operated by the Association of Universities for Research in Astronomy (AURA) under a cooperative agreement with the National Science Foundation. Pipeline processing and analyses of the data were supported by NOIRLab and the Lawrence Berkeley National Laboratory (LBNL). Legacy Surveys also uses data products from the Near-Earth Object Wide-field Infrared Survey Explorer (NEOWISE), a project of the Jet Propulsion Laboratory/California Institute of Technology, funded by the National Aeronautics and Space Administration. Legacy Surveys was supported by: the Director, Office of Science, Office of High Energy Physics of the U.S. Department of Energy; the National Energy Research Scientific Computing Center, a DOE Office of Science User Facility; the U.S. National Science Foundation, Division of Astronomical Sciences; the National Astronomical Observatories of China, the Chinese Academy of Sciences and the Chinese National Natural Science Foundation. LBNL is managed by the Regents of the University of California under contract to the U.S. Department of Energy. The complete acknowledgments can be found at <https://www.legacysurvey.org/acknowledgment/>.

Facilities:

Facility: Gaia, Pan-STARRS, DECaLS, SDSS, LaMost

REFERENCES

- Aguado, D. S., Ahumada, R., Almeida, A., et al. 2019, *ApJS*, 240, 23, doi: [10.3847/1538-4365/aaf651](https://doi.org/10.3847/1538-4365/aaf651)
- Allen, C., & Santillan, A. 1991, *RMxAA*, 22, 255

- Balbinot, E., & Gieles, M. 2018, *MNRAS*, 474, 2479, doi: [10.1093/mnras/stx2708](https://doi.org/10.1093/mnras/stx2708)
- Baumgardt, H., & Hilker, M. 2018, *MNRAS*, 478, 1520, doi: [10.1093/mnras/sty1057](https://doi.org/10.1093/mnras/sty1057)
- Baumgardt, H., & Vasiliev, E. 2021, *MNRAS*, 505, 5957, doi: [10.1093/mnras/stab1474](https://doi.org/10.1093/mnras/stab1474)
- Belokurov, V., Erkal, D., Evans, N. W., Koposov, S. E., & Deason, A. J. 2018, *MNRAS*, 478, 611, doi: [10.1093/mnras/sty982](https://doi.org/10.1093/mnras/sty982)
- Bonaca, A., & Hogg, D. W. 2018, *ApJ*, 867, 101, doi: [10.3847/1538-4357/aae4da](https://doi.org/10.3847/1538-4357/aae4da)
- Bovy, J., Bahmanyar, A., Fritz, T. K., & Kallivayalil, N. 2016, *ApJ*, 833, 31, doi: [10.3847/1538-4357/833/1/31](https://doi.org/10.3847/1538-4357/833/1/31)
- Bowden, A., Belokurov, V., & Evans, N. W. 2015, *MNRAS*, 449, 1391, doi: [10.1093/mnras/stv285](https://doi.org/10.1093/mnras/stv285)
- Callingham, T. M., Cautun, M., Deason, A. J., et al. 2022, *MNRAS*, 513, 4107, doi: [10.1093/mnras/stac1145](https://doi.org/10.1093/mnras/stac1145)
- Carlberg, R. G. 2009, *ApJL*, 705, L223, doi: [10.1088/0004-637X/705/2/L223](https://doi.org/10.1088/0004-637X/705/2/L223)
- . 2018, *ApJ*, 861, 69, doi: [10.3847/1538-4357/aac88a](https://doi.org/10.3847/1538-4357/aac88a)
- Chandrasekhar, S. 1943, *ApJ*, 98, 54, doi: [10.1086/144544](https://doi.org/10.1086/144544)
- Conroy, C., Naidu, R. P., Garavito-Camargo, N., et al. 2021, *Nature*, 592, 534, doi: [10.1038/s41586-021-03385-7](https://doi.org/10.1038/s41586-021-03385-7)
- Dai, B., Robertson, B. E., & Madau, P. 2018, *ApJ*, 858, 73, doi: [10.3847/1538-4357/aabb06](https://doi.org/10.3847/1538-4357/aabb06)
- Dey, A., Schlegel, D. J., Lang, D., et al. 2019, *AJ*, 157, 168, doi: [10.3847/1538-3881/ab089d](https://doi.org/10.3847/1538-3881/ab089d)
- Erkal, D., Belokurov, V., Bovy, J., & Sanders, J. L. 2016, *MNRAS*, 463, 102, doi: [10.1093/mnras/stw1957](https://doi.org/10.1093/mnras/stw1957)
- Erkal, D., Belokurov, V., Laporte, C. F. P., et al. 2019, *MNRAS*, 487, 2685, doi: [10.1093/mnras/stz1371](https://doi.org/10.1093/mnras/stz1371)
- Fardal, M. A., Huang, S., & Weinberg, M. D. 2015, *MNRAS*, 452, 301, doi: [10.1093/mnras/stv1198](https://doi.org/10.1093/mnras/stv1198)
- Feuillet, D. K., Feltzing, S., Sahlholdt, C. L., & Casagrande, L. 2020, *MNRAS*, 497, 109, doi: [10.1093/mnras/staa1888](https://doi.org/10.1093/mnras/staa1888)
- Gaia Collaboration, Babusiaux, C., van Leeuwen, F., et al. 2018, *A&A*, 616, A10, doi: [10.1051/0004-6361/201832843](https://doi.org/10.1051/0004-6361/201832843)
- Gaia Collaboration, Vallenari, A., Brown, A. G. A., et al. 2023, *A&A*, 674, A1, doi: [10.1051/0004-6361/202243940](https://doi.org/10.1051/0004-6361/202243940)
- Garavito-Camargo, N., Besla, G., Laporte, C. F. P., et al. 2021, *ApJ*, 919, 109, doi: [10.3847/1538-4357/ac0b44](https://doi.org/10.3847/1538-4357/ac0b44)
- Grillmair, C. J. 2009, *ApJ*, 693, 1118, doi: [10.1088/0004-637X/693/2/1118](https://doi.org/10.1088/0004-637X/693/2/1118)
- . 2019, *ApJ*, 884, 174, doi: [10.3847/1538-4357/ab441d](https://doi.org/10.3847/1538-4357/ab441d)
- . 2022, *ApJ*, 929, 89, doi: [10.3847/1538-4357/ac5bd7](https://doi.org/10.3847/1538-4357/ac5bd7)
- Grillmair, C. J., & Carlin, J. L. 2016, in *Astrophysics and Space Science Library*, Vol. 420, *Tidal Streams in the Local Group and Beyond*, ed. H. J. Newberg & J. L. Carlin, 87, doi: [10.1007/978-3-319-19336-6_4](https://doi.org/10.1007/978-3-319-19336-6_4)
- Grillmair, C. J., Freeman, K. C., Irwin, M., & Quinn, P. J. 1995, *AJ*, 109, 2553, doi: [10.1086/117470](https://doi.org/10.1086/117470)
- Gron din, S. M., Webb, J. J., Lane, J. M. M., Speagle, J. S., & Leigh, N. W. C. 2024, *MNRAS*, 528, 5189, doi: [10.1093/mnras/stae203](https://doi.org/10.1093/mnras/stae203)
- Harris, W. E. 1996, *AJ*, 112, 1487, doi: [10.1086/118116](https://doi.org/10.1086/118116)
- Helmi, A., Babusiaux, C., Koppelman, H. H., et al. 2018, *Nature*, 563, 85, doi: [10.1038/s41586-018-0625-x](https://doi.org/10.1038/s41586-018-0625-x)
- Hozumi, S., & Burkert, A. 2015, *MNRAS*, 446, 3100, doi: [10.1093/mnras/stu2318](https://doi.org/10.1093/mnras/stu2318)
- Ibata, R., Malhan, K., Martin, N., et al. 2021, *ApJ*, 914, 123, doi: [10.3847/1538-4357/abfcc2](https://doi.org/10.3847/1538-4357/abfcc2)
- Ibata, R. A., Malhan, K., & Martin, N. F. 2019, *ApJ*, 872, 152, doi: [10.3847/1538-4357/ab0080](https://doi.org/10.3847/1538-4357/ab0080)
- Irrgang, A., Wilcox, B., Tucker, E., & Schiefelbein, L. 2013, *A&A*, 549, A137, doi: [10.1051/0004-6361/201220540](https://doi.org/10.1051/0004-6361/201220540)
- Kaderali, S., Hunt, J. A. S., Webb, J. J., Price-Jones, N., & Carlberg, R. 2019, *MNRAS*, 484, L114, doi: [10.1093/mnrasl/slz015](https://doi.org/10.1093/mnrasl/slz015)
- Kallivayalil, N., van der Marel, R. P., Besla, G., Anderson, J., & Alcock, C. 2013, *ApJ*, 764, 161, doi: [10.1088/0004-637X/764/2/161](https://doi.org/10.1088/0004-637X/764/2/161)
- Katz, D., Sartoretti, P., Guerrier, A., et al. 2023, *A&A*, 674, A5, doi: [10.1051/0004-6361/202244220](https://doi.org/10.1051/0004-6361/202244220)
- Küpper, A. H. W., Balbinot, E., Bonaca, A., et al. 2015, *ApJ*, 803, 80, doi: [10.1088/0004-637X/803/2/80](https://doi.org/10.1088/0004-637X/803/2/80)
- Küpper, A. H. W., Lane, R. R., & Heggie, D. C. 2012, *MNRAS*, 420, 2700, doi: [10.1111/j.1365-2966.2011.20242.x](https://doi.org/10.1111/j.1365-2966.2011.20242.x)
- Leon, S., Meylan, G., & Combes, F. 2000, *A&A*, 359, 907, doi: [10.48550/arXiv.astro-ph/0006100](https://doi.org/10.48550/arXiv.astro-ph/0006100)
- Malhan, K., & Ibata, R. A. 2018, *MNRAS*, 477, 4063, doi: [10.1093/mnras/sty912](https://doi.org/10.1093/mnras/sty912)
- . 2019, *MNRAS*, 486, 2995, doi: [10.1093/mnras/stz1035](https://doi.org/10.1093/mnras/stz1035)
- Malhan, K., Ibata, R. A., & Martin, N. F. 2018, *MNRAS*, 481, 3442, doi: [10.1093/mnras/sty2474](https://doi.org/10.1093/mnras/sty2474)
- Malhan, K., Valluri, M., & Freese, K. 2021, *MNRAS*, 501, 179, doi: [10.1093/mnras/staa3597](https://doi.org/10.1093/mnras/staa3597)
- Malhan, K., Valluri, M., Freese, K., & Ibata, R. A. 2022, *ApJL*, 941, L38, doi: [10.3847/2041-8213/aca6e5](https://doi.org/10.3847/2041-8213/aca6e5)
- Mateu, C. 2023, *MNRAS*, 520, 5225, doi: [10.1093/mnras/stad321](https://doi.org/10.1093/mnras/stad321)
- Miyamoto, M., & Nagai, R. 1975, *PASJ*, 27, 533
- Montuori, M., Capuzzo-Dolcetta, R., Di Matteo, P., Lepinette, A., & Miocchi, P. 2007, *ApJ*, 659, 1212, doi: [10.1086/512114](https://doi.org/10.1086/512114)
- Piatti, A. E. 2018, *MNRAS*, 473, 492, doi: [10.1093/mnras/stx2471](https://doi.org/10.1093/mnras/stx2471)

- Price-Whelan, A. M., Hogg, D. W., Johnston, K. V., & Hendel, D. 2014, *ApJ*, 794, 4, doi: [10.1088/0004-637X/794/1/4](https://doi.org/10.1088/0004-637X/794/1/4)
- Rockosi, C. M., Odenkirchen, M., Grebel, E. K., et al. 2002, *AJ*, 124, 349, doi: [10.1086/340957](https://doi.org/10.1086/340957)
- Schlafly, E. F., & Finkbeiner, D. P. 2011, *ApJ*, 737, 103, doi: [10.1088/0004-637X/737/2/103](https://doi.org/10.1088/0004-637X/737/2/103)
- Schlegel, D. J., Finkbeiner, D. P., & Davis, M. 1998, *ApJ*, 500, 525, doi: [10.1086/305772](https://doi.org/10.1086/305772)
- Shipp, N., Drlica-Wagner, A., Balbinot, E., et al. 2018, *ApJ*, 862, 114, doi: [10.3847/1538-4357/aacdab](https://doi.org/10.3847/1538-4357/aacdab)
- Shipp, N., Erkal, D., Drlica-Wagner, A., et al. 2021, *ApJ*, 923, 149, doi: [10.3847/1538-4357/ac2e93](https://doi.org/10.3847/1538-4357/ac2e93)
- Sollima, A. 2020, *MNRAS*, 495, 2222, doi: [10.1093/mnras/staa1209](https://doi.org/10.1093/mnras/staa1209)
- STScI. 2022, Pan-STARRS1 DR1 Catalog, STScI/MAST, doi: [10.17909/55E7-5X63](https://doi.org/10.17909/55E7-5X63)
- Thomas, G. F., Ibata, R., Famaey, B., Martin, N. F., & Lewis, G. F. 2016, *MNRAS*, 460, 2711, doi: [10.1093/mnras/stw1189](https://doi.org/10.1093/mnras/stw1189)
- Tonry, J. L., Stubbs, C. W., Lykke, K. R., et al. 2012, *ApJ*, 750, 99, doi: [10.1088/0004-637X/750/2/99](https://doi.org/10.1088/0004-637X/750/2/99)
- Vasiliev, E. 2019, *MNRAS*, 484, 2832, doi: [10.1093/mnras/stz171](https://doi.org/10.1093/mnras/stz171)
- Vasiliev, E., & Baumgardt, H. 2021, *MNRAS*, 505, 5978, doi: [10.1093/mnras/stab1475](https://doi.org/10.1093/mnras/stab1475)
- Yang, Y., Zhao, J.-K., Tang, X.-Z., Ye, X.-H., & Zhao, G. 2023, *ApJ*, 953, 130, doi: [10.3847/1538-4357/acdee2](https://doi.org/10.3847/1538-4357/acdee2)
- Yoon, J. H., Johnston, K. V., & Hogg, D. W. 2011, *ApJ*, 731, 58, doi: [10.1088/0004-637X/731/1/58](https://doi.org/10.1088/0004-637X/731/1/58)
- Zhang, S., Mackey, D., & Da Costa, G. S. 2022, *MNRAS*, 513, 3136, doi: [10.1093/mnras/stac751](https://doi.org/10.1093/mnras/stac751)
- Zhao, G., Zhao, Y.-H., Chu, Y.-Q., Jing, Y.-P., & Deng, L.-C. 2012, *Research in Astronomy and Astrophysics*, 12, 723, doi: [10.1088/1674-4527/12/7/002](https://doi.org/10.1088/1674-4527/12/7/002)